High-Temperature Piezoelectric Characterization of Gallium Arsenide and Surface Acoustic Wave Analysis via Interdigitated Transducer Modeling

Brian D. Rummel[1], *Leonid Miroshnik*[1], *Andrew Li*[2], *Grant D. Heilman*[1], *Isaac Garcia*[1], *Lyle Alexander Menk*[3], *Ganesh Balakrishnan*[1], *Talid Sinno*[2], *Sang M. Han*[1,a]

[1]*The University of New Mexico, Albuquerque, New Mexico 87131, USA*
[2]*University of Pennsylvania, Philadelphia, Pennsylvania 19104, USA*
[3]*Sandia National Laboratories, Albuquerque, New Mexico 87185, USA*

Interdigitated transducer devices provide an advantageous platform to study stress-enhanced interfacial phenomena at elevated temperatures but require a thorough understanding of temperature-dependent material properties. In this study, the temperature dependence of the piezoelectric coefficient for gallium arsenide is determined from 22 ℃ to 177 ℃. Experimental scattering parameter responses are measured for a two-port surface acoustic wave resonator at different temperatures and piezoelectric coefficient values are extracted using a frequency-domain finite element method simulation. Device measurements are taken using an interdigitated transducer fabricated on semi-insulating GaAs(100), oriented in the ⟨110⟩ direction and device resonant frequencies are shown to decrease with increasing temperature. The experimental scattering response is used to reconcile the simulated scattering response and extract the e_{14} piezoelectric coefficient, which is shown to increase linearly with temperature. Using the extracted e_{14}, surface acoustic wave analysis is completed to study the magnitude of bulk stress values and surface displacement over the experimental temperature range produced by a standing surface acoustic wave field. Surface displacement measurements are taken at room temperature using contact-mode AFM, which corroborate the simulation predictions. The modeling results demonstrate an interdigitated transducers potential as an experimental stage to study surface and bulk stress effects on temperature-sensitive phenomena.

Introduction

Surface acoustic waves (SAWs) are mechanical waves confined to the surface of a material, with an amplitude that decays exponentially into the bulk of the substrate. In piezoelectric materials, SAWs are most often produced using an interdigitated transducer (IDT), which is constructed of two interweaving comb-shaped arrays of metal electrodes and responds to an electrical input at a specific resonant frequency. The device resonant frequency, f_r, can be predicted by $f_r = v_{SAW}/\lambda$, where λ is the acoustic wavelength, or device finger pitch, and v_{SAW} is the SAW velocity. IDT devices are often used in wireless network systems[1,2], acousto-optic technologies[3,4], and chemical[5,6], pressure[7,8], and temperature[9,10] sensors. However, they have seen minimal application for the analysis of stress-sensitive phenomena such as compositional patterning in crystalline semiconductors[11], catalytic reactions[12], and crystal growth[13] applications. Theoretical modeling has suggested the potential for periodic stress fields to enhance crystal growth and localized diffusion in compound semiconductors[11,14–18], which would be valuable for the development of next-generation semiconductor technologies. IDTs are a potential platform to study the effects of stress on semiconductor diffusion, and a rigorous understanding of these device's mechanical response is necessary for further investigation. We have previously demonstrated a 10-μm-wavelength IDT resonator device on GaAs capable of achieving up to 3 nm of displacement and nearly 0.3% strain at the substrate surface[19]. These values are within an order of magnitude of the strain necessary to alter diffusion rates, as predicted by Wu *et al.*[11], and further device improvements increase the promising prospects of this platform.

[a] Author to whom correspondence should be addressed; Email: meister@unm.edu

The tuning of an IDT's mechanical response through optimization of the device geometry is significantly aided by finite element method (FEM) modeling, as device fabrication and characterization can be an extensive and costly process. For elevated temperature modeling, knowledge of the temperature dependence for the relevant material properties is necessary. Gallium arsenide (GaAs) and its tertiary compounds have been used as a micromechanical material for piezoelectric sensors, actuators, and modulators for many decades[20–22], and is a commonly studied material for IDT devices[23–25]. The piezoelectric and elastic properties of GaAs have been thoroughly investigated for device applications at room temperatures[26–29]. Many of the material properties for GaAs, such as the elasticity matrix[30], relative permittivity[31], and thermal expansion coefficient[32] are well understood over an extensive range of temperature values. However, only room-temperature data is reported for the piezoelectric response of gallium arsenide[27,33,34], and limited data is provided for tertiary compounds at elevated temperatures[35].

The electrical and mechanical behavior of an IDT device is governed by an extension to Hooke's law that couples the mechanical stress and electric displacement of the system. The stress tensor, $\boldsymbol{T}$, and electric displacement, $\boldsymbol{D}$, within a piezoelectric domain are related to the strain tensor, $\boldsymbol{S}$, and the electric field, $\boldsymbol{E}$, by the following mathematical framework[1,25,36]:

$$T_{ij} = c^E_{ijkl} S_{kl} - e_{kij} E_k \tag{1}$$

$$D_i = e_{ijk} S_{jk} + \varepsilon_{ij} E_j \tag{2}$$

where c^E_{ijkl} are the components of the elasticity tensor for constant electric field, ε_{ij} are the components of the permittivity tensor for constant strain, and e_{ijk} are the components of the piezoelectric tensor. The piezoelectric tensor for zinc-blende crystals ($F\bar{4}3m$) has the form[37]:

$$\boldsymbol{e} = \begin{bmatrix} 0 & 0 & 0 & e_{14} & 0 & 0 \\ 0 & 0 & 0 & 0 & e_{14} & 0 \\ 0 & 0 & 0 & 0 & 0 & e_{14} \end{bmatrix} \tag{3}$$

where $\boldsymbol{e}$ is expressed in Voight notation and is only dependent on a single tensor component, e_{14}. In this study, the piezoelectric coefficient for GaAs is determined by combining scattering parameter measurements from an IDT resonator with an FEM simulation for temperatures ranging from 22 ℃ to 177 ℃. Atomic force microscopy measures the room-temperature surface displacement values for the experimental device and validates the simulation results. Standing-wave stress analysis is then completed over the range of tested temperatures to demonstrate how IDT devices are a promising platform for investigating stress-enhanced phenomena.

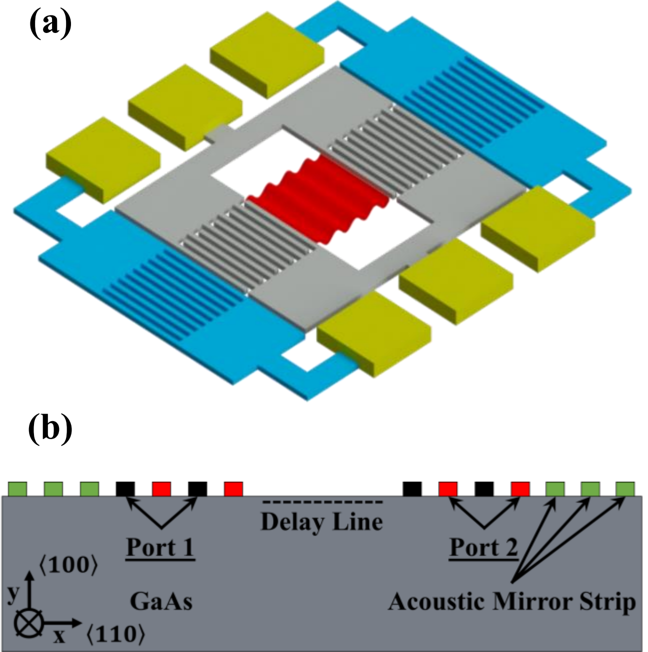

Figure 1: (a) A diagram of an IDT resonator shows a standing SAW pattern (red) is produced in the center of the IDT device (grey) and is contained by the distributed acoustic Bragg reflectors (blue). Electrical contact is made by way of wire bonding to the G-S-G pads (gold). (b) A simplified schematic of the XY-plane details the different components of the simulated IDT. The actual simulated device features 300 finger pairs, 400 mirror strips, and a 100 µm delay line region.

Experiment Description:

Device Fabrication and Experimental Procedure

The IDT used in this experiment is based on a SAW resonator design and is fabricated on semi-insulating GaAs(100), positioned such that the waves propagate in the ⟨110⟩ direction. The device consists of 300 finger pairs and an acoustic distributed Bragg reflector on both sides of the device, each comprising 200 grounded

metal strips. The finger pitch of the IDT device is 10 µm, and the grounded metal strips are spaced one-half wavelength apart. The device's aperture is 200 µm, and a 100-µm delay line region is included in the middle of the device to allow for an unimpeded standing SAW field to form. The 110-nm aluminum IDT structure is fabricated using optical lithography and electron-beam metal evaporation. A 10-nm-thick adhesion layer of titanium and a 1000-nm-thick layer of gold are additionally deposited to form ground-signal-ground (GSG) contact pads to allow for durable wire bonding. The 10-µm finger pitch of the IDT device corresponds to the SAW wavelength. A simplified schematic of the IDT resonator used in this work is shown in Fig. 1(a).

Initial device scattering response measurements are recorded using a Keysight 5247a RF Performance Network Analyzer. The resonance frequency of the device is measured to be 287.438 MHz, with an insertion loss of 1.49 dB. The device is then wire bonded to a quarter wavelength transmission line for impedance matching and powered using a Windfreak Synth NV signal generator. The device and transmission line are affixed to a 3cm-by-3cm silicon wafer with thermal epoxy for evenly distributed thermal contact during temperature response measurements. Room-temperature device measurements revealed minimal additional impedance mismatch after connecting the device to the impedance matching network as the insertion loss is measured to be 1.51 dB. The temperature response is measured by placing the device-under-test onto a hot plate and the temperature is raised slowly from 22 °C to the final temperature of 177 °C. Higher temperature values are not obtained due to the melting of the solder used to attach the SMA connectors to the quarter wavelength transmission line. The device temperature is measured using a calibrated pyrometer focused on the GaAs substrate. Contact-mode atomic force microscopy is employed to measure the surface displacement produced by the standing SAW.

COMSOL Simulation Setup

Two-dimensional device simulations are completed using COMSOL Multiphysics 5.6. Figure 1(b) depicts a simplified schematic of the simulated device. The simulated device geometry consists of two opposing sets of 150 finger pairs and 200 mirror strips. A 100-µm delay line region is included at the center of the device, mimicking the experimental device, which allows for analysis of the free-surface stress field produced by the standing SAW. The substrate and metal strips were assumed to be 200-µm-deep to emulate the experimental device aperture. The substrate is four wavelengths (40 µm) in height and utilizes a low-reflecting boundary condition and a perfectly matched domain around the bottom and sides of the perimeter to mitigate mechanical wave boundary reflections. Admittance and impedance simulations are completed by assigning a voltage terminal to each device port, while power-dependent mechanical analysis is completed by assigning power terminals in place of the voltage terminals. The acoustic mirror strips are grounded for both forms of analysis.

The piezoelectric substrate material is modeled after GaAs(100) and considers the temperature effects for the density, elasticity matrix, and relative permittivity. The material orientation for GaAs(100) is defined by a general rotation input using the Euler angle (Z-X-Z) orientation of $(90° - 45° - 90°)$ to match the experimental device orientation. The device material is modeled after aluminum and considers the temperature effects of density[38], Young's modulus[39], and Poisson's ratio[40]. Thermal expansion coefficients are incorporated for both materials to account for frequency shifts due to thermal expansion of the substrate and metal fingers[32,41]. Specific material data and a detailed description of the simulation setup can be found in the supplementary material associated with this text.

Admittance, Y_{ij}, and impedance, Z_{ij}, matrix components are simulated, and scattering responses are calculated in post-processing per the following two-port network equations[42]:

$$S_{11} = \frac{(Y_0 - Y_{11})(Y_0 - Y_{22}) + Y_{12}Y_{21}}{(Y_0 + Y_{11})(Y_0 + Y_{22}) - Y_{12}Y_{21}} \quad (5)$$

$$S_{21} = \frac{-2Y_{21}Y_0}{(Y_0 + Y_{11})(Y_0 + Y_{22}) - Y_{12}Y_{21}} \quad (6)$$

where S_{11} is the linear input port voltage reflection coefficient, S_{21} is the linear forward voltage gain, and Y_0 is the device reference impedance (50Ω). The real and imaginary parts of admittance (conductance and

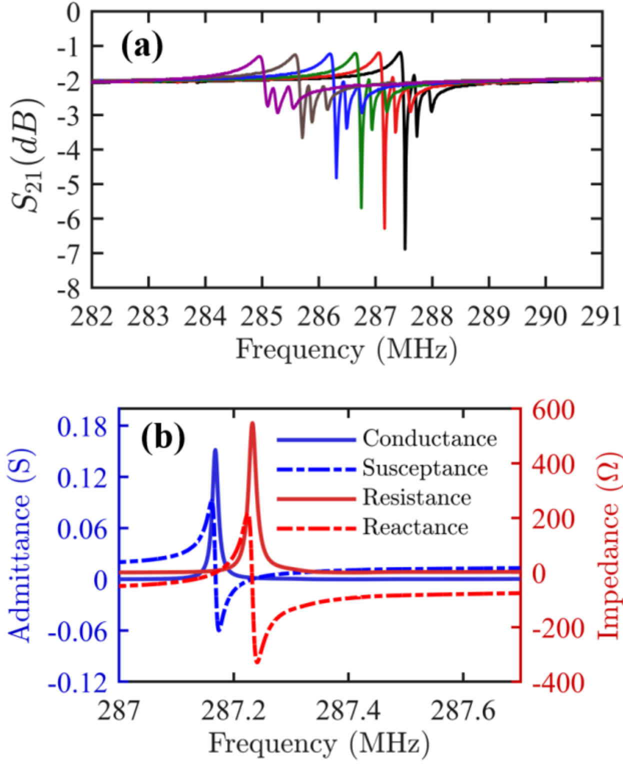

Figure 2: (a) The experimental S21 scattering response reported in decibels is shown to shift to lower frequencies with an increase in temperature. The depicted temperatures (from right to left) are 22 °C, 49 °C, 68 °C, 99 °C, 136 °C, and 177 °C. (b) The simulated real (solid line) and imaginary parts (dashed line) of admittance and impedance are used to calculate the scattering response of an interdigitated transducer and extract the temperature dependance of the piezoelectric coefficient for gallium arsenide.

susceptance) are closely associated with the resonance frequency position of an IDT device[43]. A similar association is observed for the anti-resonance position of the IDT device with respect to the real and imaginary parts of impedance (resistance and reactance)[43]. Through the electromechanical coupling coefficient, k_{ij}, the piezoelectric coefficient is related to the positions of maximum absolute device conductance and resistance[27,43]. As a result, the piezoelectric coefficient would then be sensitive to the difference between the f_r and f_a positions of an IDT device.

Results and Discussion

Experimental Measurements and Piezoelectric Characterization

Figure 2(a) shows S_{21} responses for temperature measurements ranging from 22 °C to 177 °C. A slight degradation in power transmission is observed with increasing temperature at the device resonant frequency due to a decrease in device conductance. The anti-resonant frequency's S_{21} magnitude is shown to increase in the device resistance. Additionally, a scattering response phenomenon is observed for frequencies higher than the anti-resonance frequency, which suggests that the IDT device produces additional resonant frequency modes. This effect is assumed to be due to fabrication defects or double/triple transit interference that enable higher frequency modes to exist[44], which are then further amplified by the acoustic distributed Bragg reflectors. This effect is not accounted for in the FEM simulation and therefore is not observed in the simulated scattering response.

Figure 2(b) depicts the real and imaginary values of the Y_{11} and Z_{11} matrix components for the simulated

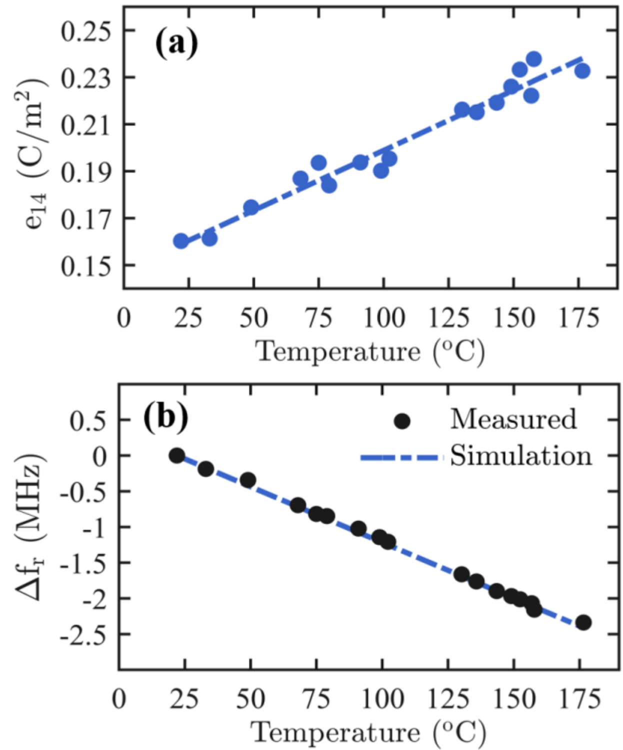

Figure 3: (a) The extracted room temperature value of e_{14} at 22 °C is 0.159 C/m^2, which agrees well with literature values. The slope of the linear fit is 5.11x10^{-4} C/m^2°C. (b) The simulated resonant frequency shift decreases linearly with temperature and matches well with measured results.

device at room temperature. The admittance matrix components, calculated for their respective temperatures, are used in determining the simulated device scattering response using Eqs. (5) and (6). The

insertion loss for the simulated device is calculated to be 0.22 dB at room temperature and decreases to 0.85 dB at 177 °C. The device performance variation is due to imperfect fabrication of the experimental devices that is not accounted for in the FEM simulation and is assumed to have a negligible impact on the positions of f_r and f_a.

The piezoelectric coefficient, e_{14}, for GaAs is readily calculated by pairing the FEM simulation to experimental measurements and are presented in Fig. 3(a). The room-temperature piezoelectric coefficient is calculated to be $0.159\ \mathrm{C/m^2}$, which is in excellent agreement with literature values[27,33,34]. As the temperature increases, the elastic and electrical energy required to alter the domain structure decreases, thus increasing the piezoelectric response of the system[45]. Therefore, the coefficient value increases to 0.238 $\mathrm{C/m^2}$ when the device temperature is increased to 177 °C. A linear fit is applied to the calculated e_{14}, which produces a reasonable fit with a slope of $5.11 \times 10^{-4}\ \mathrm{C/m^2 °C}$.

Figure 3(b) shows the agreeing experimental and simulated relative shift in resonant frequency, Δf_r, from the room temperature value for the tested range of device temperatures. The measured and simulated resonant frequencies at 22 °C are measured to be 287.438 MHz and 287.149 MHz, respectively. The simulated frequencies demonstrate a near-constant discrepancy compared to the experimental measurements over the range of tested temperatures, likely due to an imprecise representation of the experimental device within the simulation. The resonant frequency shift is attributed to various factors, most notably to the material's changing elasticity and density. As the temperature increases, the components of the elasticity matrix and the material density decrease, reducing the velocity of the SAW mode [#].

Additionally, the frequency shift can be attributed to the thermally expanded finger spacing of the interdigitated transducer. For instance, the 10-μm finger spacing is calculated to increase by approximately 8 nm at 177 °C with reference to room temperature, which accounts for nearly 230 kHz in the resonance frequency shift. Conversely, the increasing piezoelectric coefficient impedes the shift in resonant frequency such that if the piezoelectric coefficient are constant with temperature, the simulated rate of frequency shift would be even greater.

Surface Acoustic Wave Simulation and Stress Field Analysis

High-fidelity FEM modeling of device mechanical performance allows for more practical device designs and better computational data to study stress-driven effects. Utilizing the now-known temperature dependence of e_{14} for GaAs, device simulations can be completed to provide insight into the stress fields produced by standing SAWs generated by an IDT resonator. Figure 4(a) depicts the vertical displacement calculated at the standing SAW's anti-node in the simulated device's delay line region for a range of temperatures. At 22 °C, the vertical displacement reaches 6.60 nm with an applied power of 120 mW. This displacement decreases to 4.91 nm for the same applied

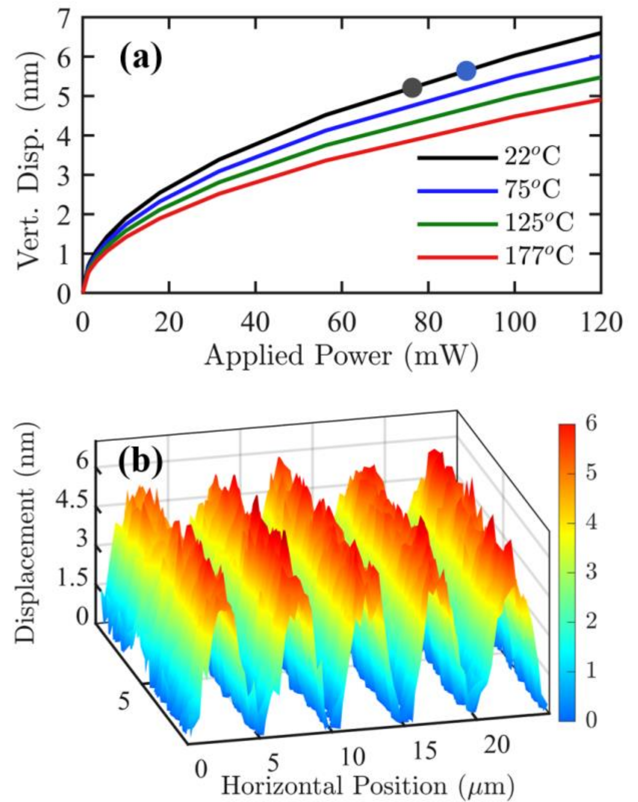

Figure 2: (a) The simulated surface displacement of the standing SAW's anti-node as a function of power. (b) Contact-mode AFM measurements validate the simulated device and depicts the absolute displacement of the standing SAW pattern.

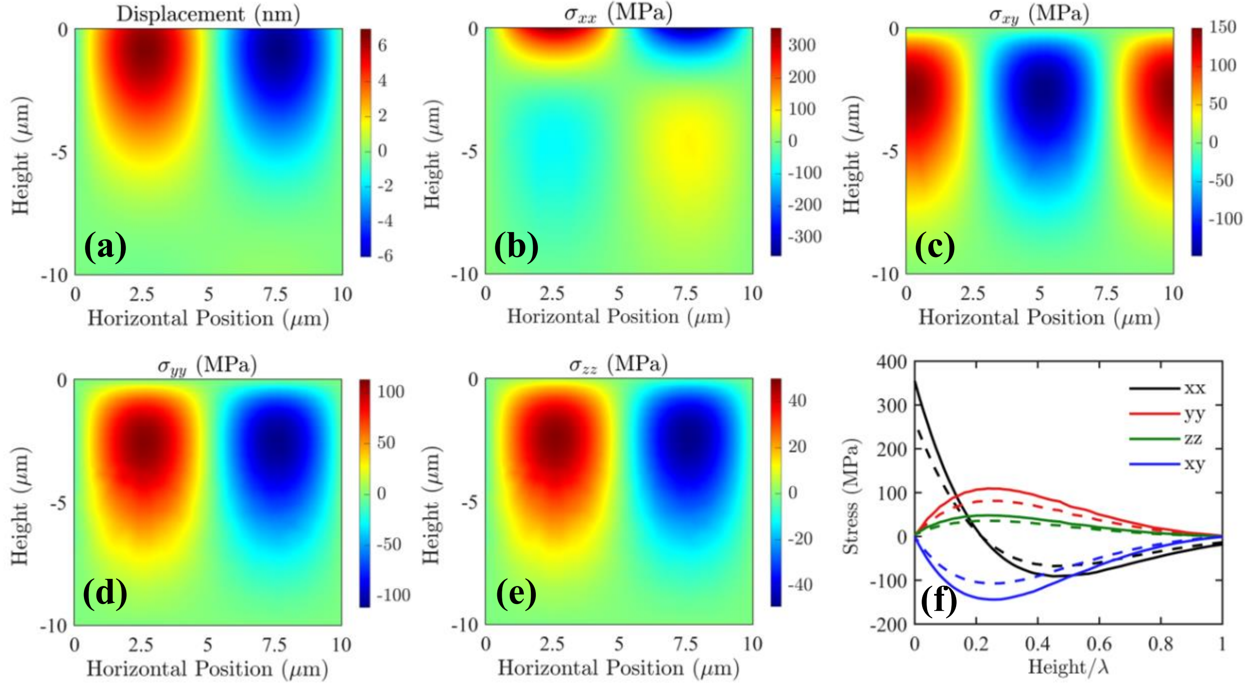

Figure 3: (a) The displacement profile illustrates the antisymmetric standing SAW over a single wavelength. The non-zero stress components, (b) σ_{xx}, (c) σ_{xy}, (d) σ_{yy}, and (e) σ_{zz} are calculated for a single snapshot at their maximum values, which switches every half period of oscillation. The displacement and stress components demonstrate the mechanical response of the standing SAW is contained to be within a single wavelength (10 µm) of the surface. (f) The stress component magnitudes decrease by approximately 26% when the temperature increases from 22 ℃ (solid line) to 177 ℃ (dashed line).

power when the simulated device temperature is increased to 177 ℃.

The 2D contact-mode AFM imaging results of the standing SAW field are shown in Fig. 4(b). Described more thoroughly in previous work[19], the dynamic behavior of the acoustic wave restricts the AFM cantilever to outline only the absolute vertical displacement of the standing SAW. AFM measurement fitting revealed a standing-wave displacement amplitude of 5.21 nm and a SAW wavelength of 10.016 µm. Due to the simulation's unaccounted impedance mismatch observed in the experimental device, the displacement values measured with the AFM do not exactly match the simulated predictions. However, the 1.29 dB difference in insertion loss between the simulated and experimental device results in a 74% efficiency, which compares well with the measured AFM results and confirms the simulation's ability to model IDT resonator devices.

Figures 5(a) portrays the displacement profile at the peak of a SAW oscillation over a single wavelength in the delay region of the device at 22 ℃. Due to the dynamic nature of standing SAW fields, the crystal domain undergoes a rapid oscillation corresponding to the frequency of the acoustic wave. The anti-node displacement will oscillate between compressive and tensile values every half temporal period. The figure depicts a single snapshot of the dynamic wave at a moment of maximum displacement and demonstrates the antisymmetric displacement profile. Figures 5(b)-(e) show the non-zero stress field component profiles for the same snapshot. Both the displacement and stress fields are characteristically contained within a single wavelength of the surface. For non-linear stress-dependent surface and bulk phenomena, different behaviors would be observed at the anti-nodal and nodal region of the standing SAW.

Figure 5(f) demonstrates how the anti-node profiles of these fields change in magnitude for the same applied power when the simulated device temperature is increased to 177 ℃. As temperature increases, the magnitudes decrease slightly for all non-zero stress components. Device components such as the quarter

wavelength transmission line, gold wire bonds, and finger-pair busbars may contribute a higher amount of resistance at elevated temperatures that may decrease the mechanical performance in a way that is not predicted by the current model. For this reason, provisions regarding the temperature response of these device component materials would need to be considered when fabricating devices.

While the temperatures for the simulated device are still lower than temperatures at which most interfacial phenomena, like atomic diffusion or crystal growth, becomes prevalent, the surface mobility of atoms can be significant [2#]. To study the effects of standing SAWs on interfacial phenomena at higher temperatures, a more temperature-robust piezoelectric substrate such as aluminum nitride or lithium niobate can be used[46,47]. SAWs can also be injected into a locally heated area within a significantly wider delay region to minimize temperature effects on the device. GaAs poses an additional problem in which arsenic sublimation becomes ubiquitous for substrate temperatures as low as 370 °C, which would impact the ability to study stress-enhanced phenomena[48]. Miroshnik *et al.* [#] demonstrate a thermal processing technique for GaAs that utilizes an encapsulant-and-sacrificial-layer method which mitigates issues associated with arsenic sublimation and pairs well with the proposed localized heating technique.

Conclusion

SAW devices offer a new platform to study the effects of surface and bulk stress on interfacial phenomena such as thermal diffusion and crystal growth and provides an opportunity for the development of new device fabrication techniques. The temperature dependence of the piezoelectric coefficient from 22 °C to 177 °C has been extracted from FEM simulations paired with experimental device response measurements. The calculated room-temperature e_{14} value of 0.159 $\mathrm{C/m^2}$ agrees well with literature values and increases linearly to 0.238 $\mathrm{C/m^2}$ when the simulated device temperature is increased to 177 °C. FEM modeling predicts the vertical displacement amplitude achieved by the standing SAW field produced in the delay-line region of the IDT that compare well with AFM measurements.

Acknowledgements

This material is based upon work supported by the National Science Foundation under Grant no. (DMR-1809095).

References

[1] C. Campbell, *Surface Acoustic Wave Devices and Their Signal Processing Applications* (1989).

[2] K. Hashimoto, *Ken-Ya Hashimoto Surface Acoustic Wave Devices in Telecommunications* (2000).

[3] C.J. Sarabalis, T.P. McKenna, R.N. Patel, R. Van Laer, and A.H. Safavi-Naeini, APL Photonics **5**, (2020).

[4] S.A. Tadesse and M. Li, Nat. Commun. **5**, 1 (2014).

[5] J. Devkota, P.R. Ohodnicki, and D.W. Greve, Sensors (Switzerland) **17**, 13 (2017).

[6] E. Benes, M. Groschl, W. Burger, and M. Schmid, Sensors Actuators A **1**, (1995).

[7] P. Nicolay, H. Chambon, G. Bruckner, C. Gruber, S. Ballandras, E. Courjon, and M. Stadler, Sensors (Switzerland) **18**, (2018).

[8] T. Hoang, Design and Realization of SAW Pressure Sensor Using Aluminum Nitride, L'Universite Joseph Fourier, 2009.

[9] C. Fu, Y. Ke, M. Li, J. Luo, H. Li, G. Liang, and P. Fan, Sensors (Switzerland) **17**, (2017).

[10] L.M. Reindl and I.M. Shrena, IEEE Trans. Ultrason. Ferroelectr. Freq. Control **51**, 1457 (2004).

[11] C. Wu, V.Y. Zaitsev, and L. V. Zhigilei, Appl. Phys. Lett. **103**, (2013).

[12] B. von Boehn, M. Foerster, M. von Boehn, J. Prat, F. Macià, B. Casals, M.W. Khaliq, A. Hernández-Mínguez, L. Aballe, and R. Imbihl, Angew. Chemie - Int. Ed. (2020).

[13] M.J. Aziz, P.C. Sabin, and G.Q. Lu, Phys. Rev. B **44**, 9812 (1991).

[14] M. Schroeder and D.E. Wolf, Surf. Sci. **375**, 129 (1997).

[15] M. Rosini, P. Kratzer, and R. Magri, J. Phys. Condens. Matter **21**, (2009).

[16] M. V. Shugaev, A.J. Manzo, C. Wu, V.Y. Zaitsev, H. Helvajian, and L. V. Zhigilei, Phys. Rev. B - Condens. Matter Mater. Phys. **91**, 1 (2015).

[17] C. Taillan, N. Combe, and J. Morillo, Phys. Rev. Lett. **106**, 1 (2011).

[18] C. Taillan, N. Combe, and J. Morillo, Phys. Rev. B **96**, 1 (2017).

[19] B.D. Rummel, L. Miroshnik, M. Patriotis, A. Li, T.R. Sinno, M.D. Henry, G. Balakrishnan, and S.M. Han, Appl. Phys. Lett. **118**, 1 (2021).

[20] J.L. Robert, V. Mosser, and S. Contreras, Transducers '91 294 (1991).

[21] J.-F. Manceau, M. Billot, V. Lacour, and T. Leblois, C001 (2015).

[22] J.P.R. David, E.A. Khoo, A.S. Pabla, J. Woodhead, R. Grey, and G.J. Rees, Des. Fabr. Charact. Photonic Devices **3896**, 163 (1999).

[23] M.M. De Lima, W. Seidel, H. Kostial, and P. V. Santos, J. Appl. Phys. **96**, 3494 (2004).

[24] B. Dong and M.E. Zaghloul, Nanoscale Adv. **1**, 3537 (2019).

[25] R. Mathew, Creating and Imaging Surface Acoustic Waves on GaAs, 2009.

[26] W.A. Brantley, J. Appl. Phys. **44**, 534 (1973).

[27] S. Adachi, J. Appl. Phys. **58**, (1985).

[28] J. Soderkvist and K. Hjort, J. Micromechanics Microengineering **4**, 28 (1994).

[29] K. Fricke, J. Appl. Phys. **70**, 914 (1991).

[30] M. Levinshtein, S. Rumyantsev, and M. Shur, *Handbook Series on Semiconductor Parameters, Volume 1* (World Scientific, 1996).

[31] T. Lu, G.H. Glover, and K.S. Champlin, Appl. Phys. Lett. **13**, 404 (1968).

[32] E.D. Pierron, D.L. Parker, and J.B. McNeely, J. Appl. Phys. **38**, 4669 (1967).

[33] J.B. McKitterick, Phys. Rev. B **28**, 7384 (1983).

[34] G. Arlt and P. Quadflieg, Phys. Status Solidi **25**, 323 (1968).

[35] J.J. Sánchez, J.I. Izpura, J.M.G. Tijero, E. Muñoz, S. Cho, and A. Majerfeld, J. Appl. Phys. **91**, 3002 (2002).

[36] B.A. Auld, *Acoustic Fields and Waves in Solids - Volume 1* (John Wiley and Sons, Inc., 1973).

[37] J.F. Nye, *Physical Properties of Crystals* (Oxford University Press, 1987).

[38] P. Foteinopoulos, A. Papacharalampopoulos, and P. Stavropoulos, CIRP J. Manuf. Sci. Technol. **20**, 66 (2018).

[39] P.T. Summers, Y. Chen, C.M. Rippe, B. Allen, A.P. Mouritz, S.W. Case, and B.Y. Lattimer, Fire Sci. Rev. **4**, (2015).

[40] K. Davoudi, Scr. Mater. **131**, 63 (2017).

[41] J. Carvill, in *Mech. Eng. Data Handb.* (1993), pp. 218–266.

[42] D.M. Pozar, *Microwave Engineering; 4th Edition*, 4th ed. (John Wiley and Sons, Inc., 1998).

[43]IEEE Trans. Sonics Ultrason. **31**, 8 (1984).

[44] M. Powlowksi, F. Sfigakis, and N. Kim, Jpn. J. Appl. Phys. (2019).

[45] R.G. Sabat, W. Ren, G. Yang, and B.K. Mukherjee, IEEE Int. Symp. Appl. Ferroelectr. 612 (2007).

[46] B.R. Tittmann, D.A. Parks, S.O. Zhang, B. Tittman, D.A. Parks, and O. Zhang, 13th Int. Symp. Nondestruct. Characterisation Mater. 20 (2013).

[47] T. Kim, J. Kim, R. Dalmau, R. Schlesser, E. Preble, and X. Jiang, IEEE Trans. Ultrason. Ferroelectr. Freq. Control **62**, 1880 (2015).

[48] J.R. Arthur, Surf. Sci. **43**, 449 (1974).